



# Generation of medical isotopes $^{47}\text{Sc}$ , $^{67}\text{Cu}$ through laser-induced ( $\gamma$ , p) reaction

Jian-Yao Zhang<sup>1,2</sup> · Di Wu<sup>1,2</sup> · Hao-Yang Lan<sup>1,2</sup> · Huan-Gang Lu<sup>1,2</sup> · Jia-Xin Liu<sup>1,2</sup> · Jian-Feng Lv<sup>1,2</sup> · Mei-Zhi Wang<sup>1,2</sup> · Xue-Qing Yan<sup>1,2</sup>

Received: 28 March 2024 / Revised: 17 May 2024 / Accepted: 11 June 2024 / Published online: 21 October 2024

© The Author(s), under exclusive licence to China Science Publishing & Media Ltd. (Science Press), Shanghai Institute of Applied Physics, the Chinese Academy of Sciences, Chinese Nuclear Society 2024

## Abstract

Short-lived medical isotopes and their generators are typically produced in nuclear reactors and cyclotrons that require extensive facilities. However, considering the environmental concerns and economic costs of these traditional approaches, modern laser technology, which provides extremely strong electric fields within tabletop-sized areas, can serve as a potential supplementary method. Focusing specifically on the ( $\gamma$ , p) generation of the vital medical isotopes  $^{47}\text{Sc}$  and  $^{67}\text{Cu}$ , we used both experimental results and PIC-GEANT4 simulations to demonstrate that laser-induced photonuclear reaction is a promising method for isotope production. We developed a model capable of calculating isotope yields under various laser conditions and acceleration mechanisms. The findings revealed that a 200 TW laser can sufficiently produce diagnostic amounts of  $^{47}\text{Sc}$  and  $^{67}\text{Cu}$ , while simultaneously providing high specific activity, which is significant in medical applications for improving treatment efficacy, enhancing image resolution, and reducing side effects.

**Keywords** Photonuclear reaction · Laser-driven  $\gamma$ -Ray · Medical isotope

## 1 Introduction

The rapid development of laser technology and laser-plasma acceleration techniques has provided high-quality electron bunches with vastly adjustable energies, leading to effective laser-based X-ray and  $\gamma$ -ray sources [1]. This provides extensive opportunities in the photonuclear field such as medical isotope production [2–4], nuclear waste transmutation [5–7], isomer generation [8], and photonuclear data measurements [9–12]. In these applications, electrons are accelerated by ultrafast laser pulses, typically through laser wakefield acceleration (LWFA) or direct laser acceleration (DLA), and bombarding a bremsstrahlung converter, leading to photon emission and subsequent photonuclear reactions with the target material. Since most responses are distributed

within the giant dipole resonance (GDR) region, the laser-driven  $\gamma$  source must maximize photon production within this energy range.

Medical radioisotopes can generally be obtained in two ways: nuclear reactions in particle accelerators and the fission of highly enriched uranium in nuclear reactors, each of which has non-negligible shortcomings [13]. Cyclotrons are primarily employed to produce short-lived, neutron-deficient,  $\beta^+$ -emitting radioisotopes. However, these radioisotopes must be used promptly after production owing to their short half-lives. Therefore, many medical centers must spend considerable amounts of money and space to maintain their own accelerators. By contrast, research reactors primarily manufacture long-lived  $\beta^-$ - and  $\gamma$ -ray-emitting radioisotopes. They often need to be distributed before use. However, the vast amount of nuclear waste generated during the production and transport of highly radioactive materials over extended distances afterward can cause environmental contamination risks. Therefore, a new, compact, environmentally safe, and cost-effective technology for the production of radioisotopes is required.

Photonuclear reactions using laser-driven  $\gamma$  photons have long been considered as promising alternatives for isotope

✉ Xue-Qing Yan  
x.yan@pku.edu.cn

<sup>1</sup> State Key Laboratory of Nuclear Physics and Technology, School of Physics, CAPT, Peking University, Beijing 100871, China

<sup>2</sup> Beijing Laser Acceleration Innovation Center, Beijing 101407, China

production [14, 15]. The rapid progress in laser manufacturing technology has made high-intensity and high-repetition-rate laser systems smaller and more cost-effective, allowing for the decentralized production of medical isotopes, thus mitigating issues arising during transportation [16]. Bremsstrahlung  $\gamma$ -ray reaction routes produce very little radioactive waste, making them environmentally safe. Moreover, the narrow focal spot of the laser confines the reaction to a small area, which significantly increases the specific activity of the isotope.

This study focused on the  $(\gamma, p)$  generation of two selected medical isotopes:  $^{47}\text{Sc}$  and  $^{67}\text{Cu}$ . Using the  $(\gamma, p)$  reaction to produce radioisotopes has an additional advantage because this process involves element transfer, making it possible to extract and enrich the target isotopes through chemical mechanisms that are more convenient and less expensive than physical centrifugal separation.  $^{47}\text{Sc}$  and  $^{67}\text{Cu}$  were both highlighted as promising theranostic radionuclides by the recent IAEA Coordinated Research Project (CRP) on "Therapeutic Radiopharmaceuticals Labelled with New Emerging Radionuclides ( $^{67}\text{Cu}$ ,  $^{186}\text{Re}$ ,  $^{47}\text{Sc}$ )" (IAEA CRP no. F22053). However, their limited availability owing to a lack of widely established production methods remains a problem [17, 18].  $^{47}\text{Sc}$  ( $T_{1/2} = 3.3$  d) is an excellent theranostic radionuclide considering its 100%  $\beta^-$  emitter nature, and the combination of  $^{44}\text{Sc} + ^{47}\text{Sc}$  is gaining increasing attention as an excellently matched pair of nuclides for positron emission tomography (PET) imaging and radionuclide therapy [17]. Owing to the location of  $^{47}\text{Sc}$  in the nuclide chart, the photonuclear reaction  $^{48}\text{Ti}(\gamma, p)^{47}\text{Sc}$  appears to be the most promising method for its production [19].  $^{\text{nat}}\text{Ti}$  contains 74% of  $^{48}\text{Ti}$ , so either  $^{\text{nat}}\text{Ti}$  or enriched  $^{48}\text{Ti}$  may be used as the irradiation target.  $^{67}\text{Cu}$  ( $T_{1/2} = 61.8$  h) is one of the five copper isotopes that can be used in nuclear medicine. Its simultaneous emissions of  $\beta^-$  radiation (mean  $\beta^-$  energy: 141 keV;  $E_{\beta^- \text{max}}$ : 562 keV) and  $\gamma$ -rays (185 keV) are useful for therapeutic treatments and single-photon emission computed tomography (SPECT) imaging [20]. Because Cu is present in the human body,  $^{67}\text{Cu}$  is also considered a possible marker for studying the Cu distribution in the body for different diseases [21, 22]. Although this radionuclide can be produced in cyclotrons via the  $^{68}\text{Zn}(\gamma, p)^{67}\text{Cu}$  reaction at 100 MeV, only a few accelerators worldwide are suitable for this task [18]. Therefore, the photonuclear reaction  $^{68}\text{Zn}(\gamma, p)^{67}\text{Cu}$  is a suitable choice. However, enriched targets may be needed, since  $^{\text{nat}}\text{Zn}$  contains only 19% of  $^{68}\text{Zn}$ .

Herein, we employ both experiments and simulations to explore the potential for producing the radioisotopes  $^{47}\text{Sc}$  and  $^{67}\text{Cu}$  via laser-induced  $(\gamma, p)$  reactions. Section 2 introduces the experimental setup and the obtained results. We cross-validated the experimental outcomes with our simulation results and optimized the target parameters to achieve the theoretical maximum yield under the experimental

electron conditions in Sect. 3. In Sect. 4, further optimization of the electron acceleration mechanism indicated that the maximum yield is achievable with a typical 200 TW laser, similar to CLAPA. We demonstrated that the activity and specific activity can be sufficiently high under this scheme with the help of upcoming kHz lasers. The investigation of laser-induced photonuclear reactions as a viable means of producing medically essential isotopes marks a significant leap toward a compact, environmentally safe, and economically feasible technology.

## 2 Experiment

A preliminary experiment was conducted at the Compact Laser Plasma Accelerator (CLAPA) laboratory of Peking University, which has a 200 TW 5 Hz Ti:sapphire laser system, to validate the feasibility of this laser-induced photonuclear method and estimate its efficiency. As shown in Fig. 1a, monochromatic electrons accelerated by LWFA flew past various detectors before reaching the converter, and the subsequently generated bremsstrahlung photons underwent  $(\gamma, p)$  reactions with the target. During the experiment, the laser system was operated at moderate energy (1.8 J on the gas target), delivering laser pulses with a focused intensity of approximately  $1.5 \times 10^{19}$  W/cm<sup>2</sup> and a full width at half maximum (FWHM) duration of 30 fs. The laser beam was set to  $21 \mu\text{m} \times 23 \mu\text{m}$  FWHM at the nozzle.

The gas jet emitted from the nozzle comprised 99.9% He. After being expelled at a pressure of 30 bar, it underwent supersonic expansion and LWFA upon encountering a laser pulse. The electron charge was measured using a Turbo Integrating Current Transformer (Turbo-ICT). A 20 cm  $\times$  23 cm dipole magnet with a 0.8 T peak magnetic field was placed 100 cm away from the gas target to measure the electron energy spectrum. A scintillator ( $\text{Gd}_2\text{O}_2\text{S} : \text{Tb}$ ) was placed at the entrance and exit of the magnet. A CCD imaging system with two cameras recorded the divergence and pointing angles of the beams at the entry (see the sample image in Fig. 1b), and the energy spectrum at the exit (see the sample image in Fig. 1c). Because the decay signals of both isotopes were within the 150 keV – 200 keV range and will undergo significant self-absorption within the target material, we chose our targets as 2 cm  $\times$  2 cm squares made from  $^{\text{nat}}\text{Ti}$  and  $^{\text{nat}}\text{Zn}$  with a thickness of 2 mm, which also secured radiation safety during experiments. A  $^{\text{nat}}\text{Ta}$  converter with the same shape as the target was placed at the magnet entrance, directly facing the target, which was positioned at the magnet exit. Setting the laser repetition rate at 0.2 Hz to maintain the vacuum, we irradiated each target for 20 min with approximately 240 laser shots. Electron parameters were then analyzed, and we found that the

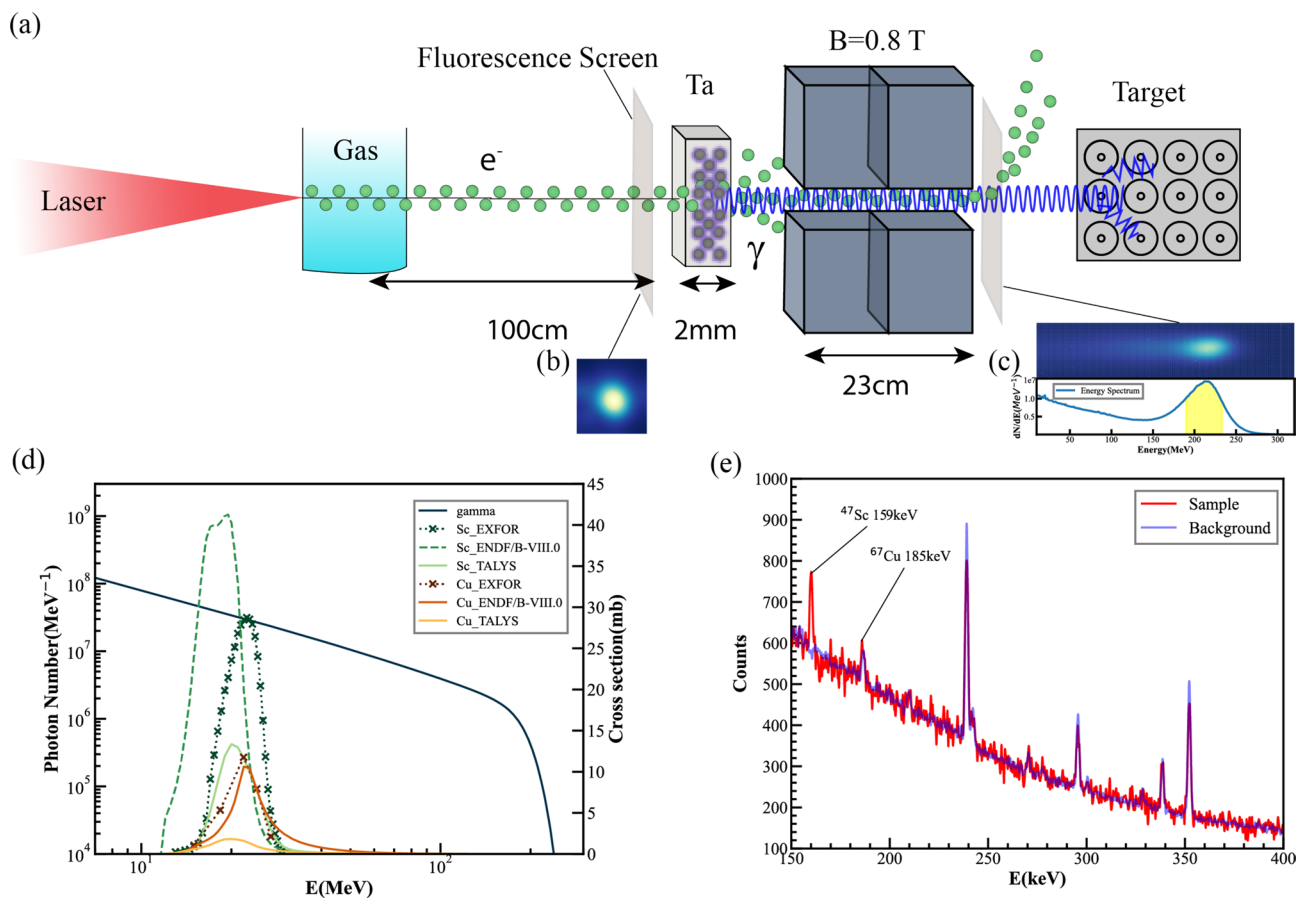


**Fig. 1** (Color online) Experimental results. **a** Schematic of the experimental setup. **b** Electron beam spot on the front fluorescence screen. The electron scattering angle is deduced to be approximately 4 mrad. **c** Electron energy spectrum on the back fluorescence screen, featuring a quasi-monoenergetic peak at 220 MeV, and the energy region over

10 MeV has an approximately 300 pC charge. **d** Geant4 simulated the gamma spectrum using the electron energy spectrum and cross sections measured from various sources. **e** Spectrum on the HPGe detector. The red line is the detector signal with the sample, and the blue line is the accumulated background radiation

electrons with energies exceeding 10 MeV typically carried charges ranging from 250 pC – 350 pC while featuring a quasi-monoenergetic peak at around 220 MeV, and the charge within this peak was approximately 110 pC (see Fig. 1c).

Radioactive nuclides were detected by recording their characteristic decay signals (159 keV for  $^{47}\text{Sc}$  and 185 keV for  $^{67}\text{Cu}$ ) on a high-purity germanium (HPGe) detector shielded in Pb bricks. The samples were arranged side-by-side on the detector probe for 200 min the day after

irradiation. The detector efficiencies were calibrated with  $^{152}\text{Eu}$  and  $^{60}\text{Co}$  sources and were finally determined by GEANT4 simulations according to the actual spatial position during detection. The detection results, along with the background radiation spectrum, are shown in Fig. 1e. Both characteristic signals were significant considering the measurement uncertainty. The net counts of the characteristic signals after subtracting the background radiation are listed in Table 1. A total of 801 and 84 signals were obtained for  $^{47}\text{Sc}$  and  $^{67}\text{Cu}$ , respectively.

**Table 1** Experiment results

Isotopes	$\tau_{1/2}$ (h)	Decay mode	Reaction	Signals	Yield (total)	Yield (single shot)	Calculation (single shot)
$^{47}\text{Sc}$	80.4	$\beta^-$ , 159 keV(100%)	$^{48}\text{Ti} (\gamma, p)$	801( $\pm$ 68)	$1.1(\pm 0.2) \times 10^7$	$4.5(\pm 1.7) \times 10^4$	$6.2 \times 10^4$
$^{67}\text{Cu}$	61.7	$\beta^-$ , 185 keV(49%)	$^{68}\text{Zn} (\gamma, p)$	84( $\pm$ 13)	$9.0(\pm 2.2) \times 10^5$	$7.7(\pm 3.1) \times 10^3$	$5.7 \times 10^3$

These data can be used to deduce the average yield from a single-shot laser shot, denoted as  $N$ , which can be derived using the following equation:

$$N_{\text{tot}}\eta(\exp(-\lambda t_1) - \exp(-\lambda t_2))\Gamma = N_{\text{count}}/\tau, \quad (1)$$

$$N_{\text{tot}} = N \sum_{i=0}^{fT} \exp\left(-\lambda\left(T - \frac{i}{f}\right)\right) \approx NfT. \quad (2)$$

$N_{\text{count}}$  and  $N_{\text{tot}}$  are the total number of isotopes after radiation,  $\eta$  is the absolute full-energy efficiency of the HPGe detector considering self-absorption and the solid angle,  $\lambda$  is the decay constant,  $\Gamma$  is the branching ratio of the characteristic  $\gamma$  energy,  $\tau$  is the dead time correction of the data acquisition system,  $t_1$  and  $t_2$  are the respective start and end times of measurement, and  $f$  and  $T$  represent the repetition rate of the laser pulse and the total radiation time. The results are  $4.5(\pm 1.7) \times 10^4$  for  $^{47}\text{Sc}$  and  $7.7(\pm 3.1) \times 10^3$  for  $^{67}\text{Cu}$  (see Table 1). The uncertainty in this result can be attributed to three sources: the measurement process of the detector, uncertainties in the half-life and branching ratio, and fluctuations in the laser and electron parameters during repetitive laser radiation.

Determining the photonuclear reaction cross section is a complicated task, and the current experimental data are only valid under specific conditions. We theoretically estimated the isotope yield to validate our experimental results and determine the most reliable cross sections to be used in the subsequent simulation. The analytical estimation of the  $(\gamma, p)$  reaction yield can be obtained from

$$N = n_a d \int_{E_{\text{th}}}^{\infty} dE \sigma(E) \frac{dN_\gamma}{dE}, \quad (3)$$

where  $n_a$  and  $d$  are the target atomic density and target thickness,  $N_\gamma$  is the number of gamma photons,  $E$  and  $E_{\text{th}}$  are electron energy and the threshold energy of the  $(\gamma, p)$  reaction, and  $\sigma(E)$  is the reaction cross section at photon energy  $E$ . Because our targets had a thickness of only 512 mm, Eq. (3) neglects the effect of gamma flux attenuation. In our estimation, the corresponding  $\sigma(E)$  for isotope generation was evaluated using TALYS-1.9 [23], which is compared with the experimental cross sections obtained from the EXFOR database in Fig. 1d. As we can see, the experimental cross sections comprise only a few data points and deviate significantly from the theoretical values, proving the need for validation using the data in this study. However, theoretical calculations and numerical simulations for resonance-induced radiation are already well established. Therefore, the bremsstrahlung gamma spectrum is acquired by performing Monte Carlo simulations using Geant4 [24]. Under QGSP\_BERT\_HP physics lists, incident electrons whose energy distribution follows the experimentally measured

energy spectrum strike the converter, and the generated bremsstrahlung photons are collected. Figure 1d shows the representative energy spectrum for an average electron charge of 300 pC. The results obtained from Eq. (3) are  $6.2 \times 10^4$  for  $^{47}\text{Sc}$  and  $5.7 \times 10^3$  for  $^{67}\text{Cu}$ . Our theoretical estimation aligns with the experimental results within the permissible margin of experimental uncertainty (see Table 1); therefore, we can confidently proceed with this cross section in the following section.

### 3 Target optimization

The radionuclide activity produced by laser-induced bremsstrahlung  $\gamma$  rays depends on many parameters, including electron current, electron energy, the converter material, geometry, converter thickness, and the target. The laser acceleration process dictates various electron properties: the interaction between the electrons and the converter determines the gamma properties, and the  $(\gamma, p)$  reactions in the target determine the radionuclide yield and distribution. In this section, while maintaining the experimental acceleration conditions, the gamma generation and photonuclear reaction processes are optimized by refining the parameters of the converter and the target. The laser acceleration process is discussed in the next section.

The key component of the gamma generation process is the bremsstrahlung converter, which transforms electron energy into photon energy. The conversion efficiency between the electron and photon energies depends strongly on the atomic number of the material; therefore, converters are usually made of high- $Z$  metals such as tantalum or tungsten. The bremsstrahlung interaction generates a broad spectrum of photon energies, ranging from zero to the energy of the incoming electron beam. This photon spectrum exhibits a gradual decrease in the photon flux as the photon energy increases, tapering off entirely at the maximum photon energy. In our case, photons within the energy range of 8 MeV – 35 MeV hold particular significance owing to the substantial enhancement of photonuclear cross sections in this domain of the giant dipole resonance. Because bremsstrahlung is produced and attenuated by the converter, the optimal converter thickness can be determined for any given electron beam energy and specific converter material. This optimum thickness corresponds to a peak in the number of photons within the critical energy range, signifying the maximal yield of the photons of interest. Using tantalum as the conversion material and fixing the electron charge at 100 pC, we conducted a parameter scan of the converter thicknesses across various electron energies using the Geant4 simulation method. The number of photons exiting from the back of the converter when choosing different thicknesses and electron energies is shown in Fig. 2. The

**Table 2** Optimized generation

Isotopes	Target	Atoms per shot	Time (h)	Rate (kHz)	Activity (MBq)	Specific activity (MBq/g)
<sup>47</sup> Sc	<sup>nat</sup> Ti	6.1 × 10 <sup>6</sup>	8	1	412	26
<sup>67</sup> Cu	<sup>68</sup> Zn	1.9 × 10 <sup>6</sup>	15	1	306	16

optimal thickness of the conversion material increases as the electron energy increases, as shown by the white dashed line. For instance, at 100 MeV, the optimal thickness was approximately 8 mm, extending to 10 mm at 200 MeV. Therefore, for LWFA, the thickness of the conversion material can be approximated based on the location of the electron quasi-monoenergetic peak. As the electron energy increases, the growth rate of GDR photons gradually declines, which naturally leads us to explore the relationship between electron energy and isotope yield in the subsequent paragraph.

The electron parameters validate the effectiveness of the laser acceleration process and determine the conditions of the photonuclear reactions, making electrons the focal point of the entire scheme. Suppose we know the reaction yield caused by monoenergetic incident electrons of varying energies and the energy spectrum of laser-accelerated electrons. In this case, we could quickly compute the isotope yield under different laser parameters using the following integration:

$$N = \int_{E_{th}}^{\infty} dE \frac{dY(E)}{dN_e} \frac{dN_e}{dE}, \tag{4}$$

where  $N_e$  is the number of electrons,  $E_{th}$  is the threshold energy of the reaction,  $Y(E)$  is the isotopic yield at energy  $E$ . Thus,  $dN_e/dE$  represents the energy spectrum, and  $dY(E)/dE$  denotes the number of isotopes produced by a unit quantity of electrons at energy  $E$ . In the experiment, the electrons were deflected away by a dipole magnet after passing through the converter, thus eliminating the need to consider subsequent reactions if the electrons strike the target directly. We conducted a Geant4 simulation, fixing the converter thickness at 11 mm to match the quasi-monoenergetic peak of the experimental electron energy spectrum (see Fig. 2) to obtain  $dY(E)/dE$  by using the method verified at the end of Sect. 2 (also shown in Table 1). Considering the mean free path of 30 -MeV energy gamma photons within the target material, a cylindrical target with a radius of 2 cm and a length of 15 cm would sufficiently cover the region where most reactions occur, as shown in Fig. 4. In addition, enriched targets are employed to improve the generation of <sup>67</sup>Cu due to the low abundance of <sup>68</sup>Zn in <sup>nat</sup>Zn. The relationship between the electron energy and isotope yield is shown in Fig. 3, and we found that increasing the energy of the electrons logarithmically enhances the isotope

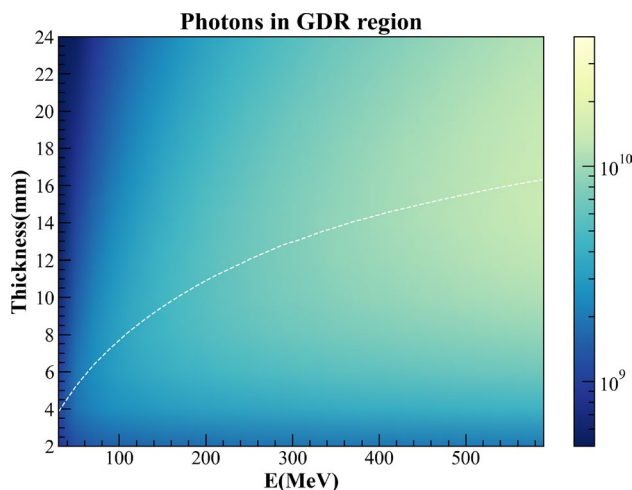


**Fig. 2** (Color online) The number of GDR photons from the backside of the converter when electrons with a charge of 100 pC irradiate the Ta converter. The white dashes represent the optimal thicknesses corresponding to different energies

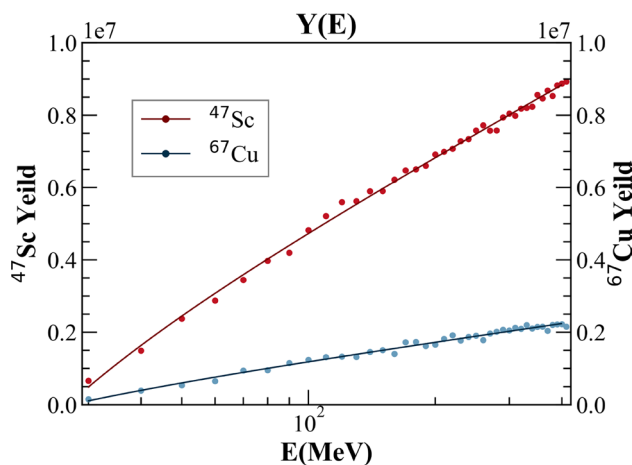


**Fig. 3** (Color online) Reaction yield due to monoenergetic incident electrons of varying energies. The red and blue dots correspond to the simulated results for Sc and Cu, while the solid red and blue lines represent the logarithmic curve fittings for each

yield. Substituting these results into Eq. 4, we can calculate the production of  $6.1 \times 10^6$  <sup>47</sup>Sc and  $1.9 \times 10^6$  <sup>67</sup>Cu under the experimental electron spectrum (300 pC over 10 MeV with a quasi-monoenergetic peak at 220 MeV). To provide

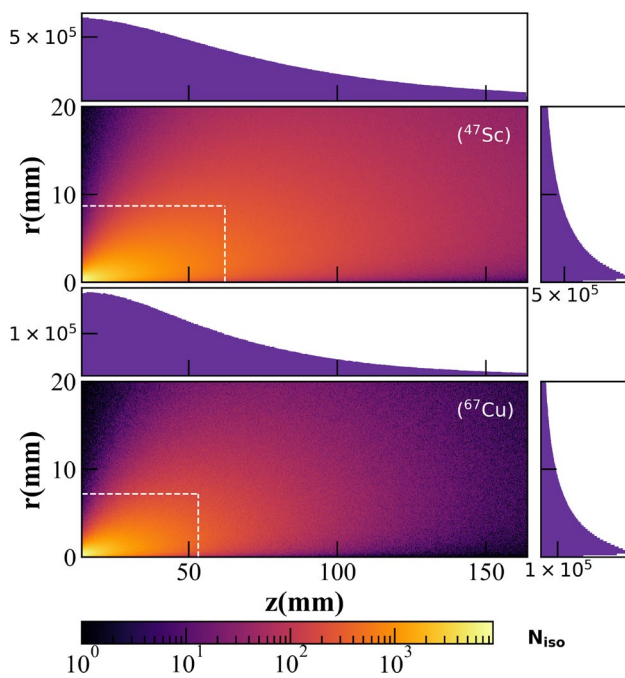


**Fig. 4** (Color online) Isotope distribution in the cylindrical source after one laser shot. The image resolution is  $0.1 \text{ mm} \times 0.1 \text{ mm}$ , and each shaded point on the two-dimensional heatmap represents the quantity of all isotopes within a circular ring. The white dashed line indicates the scheme that maximizes the specific activity while retaining over half of the radioactivity

a typical medical dose of 300 MBq, 8 h irradiation with a 1 kHz repetition rate laser is required for  $^{47}\text{Sc}$ , while 15 h irradiation with a 1 kHz repetition rate laser is required for  $^{67}\text{Cu}$ . The results are shown in Table 2.

A primary advantage of laser-induced photonuclear radioisotope generation is that all reactions occur within a confined area owing to the small size of the laser focal spot and electron beam. This implies that we can achieve a significantly higher specific activity required for most medical radioisotopes if suitable target dimensions are selected. For example, in LWFA, the bubble size is typically less than  $10 \mu\text{m}$  [25], implying that the electron-source size does not exceed this dimension. We conducted a simulation to obtain the optimal target shape, in which the input electron spectrum matched that obtained experimentally. According to our experimental measurements, we set the electron-source size to  $5 \mu\text{m}$  and the divergence angle to 4 mrad. We then obtained the isotope distribution after one laser shot, as shown in Fig. 4; the white dashed line indicates the scheme that maximizes the specific activity while retaining over half of the radioactivity; we stick to a cylindrical shape for engineering property considerations. Following the irradiation scheme mentioned in the previous paragraph, the specific activity can ultimately accumulate to 26 MBq/g for  $^{47}\text{Sc}$ , and 16 MBq/g for  $^{67}\text{Cu}$  under the experimental electron

spectrum (300 pC over 10 MeV with a quasi-monoenergetic peak at 220 MeV). This is more than sufficient for typical medical use [15].

## 4 Electron optimization

We optimized the converter and target properties in the previous section to enhance the isotope yield under the experimental electron conditions. Next, we demonstrate that by adjusting the mechanism of the laser acceleration process, the improvement in electron charge and energy significantly reduces the repetition frequency requirements, leading us to be much closer to practical applications.

The LWFA regime is prevalent for electron acceleration in underdense plasma conditions, as was the case in our experiment. As the plasma density increases and gradually approaches the critical density, the direct laser acceleration (DLA) regime assumes dominance. Previous studies [26, 27] have indicated that in near-critical density plasmas, by choosing a matched size that maximizes the conversion efficiency from laser to energetic electrons, a typical 200 TW laser can generate high-energy ( $>10 \text{ MeV}$ ) electrons on the order of 10 nC through the hybrid of these two acceleration mechanisms. The matching conditions can be expressed as [27]

$$k_p R \simeq k_p \omega_0 = 2\sqrt{a_0}, \quad (5)$$

where  $k_p = 2\pi/\lambda_p$  represents the wave vector of the plasma wave and  $R$  is the blowout radius.  $\omega_0$ , which satisfies this equation, can result in an equilibrium between the transverse ponderomotive force and the force of the ion channel, which is beneficial for long-distance acceleration in both the LWFA and DLA regimes.

The open-source PIC code SMILEI [28] is used to simulate the electron acceleration process. The 3D simulations assume a linearly polarized femtosecond Gaussian laser pulse with a wavelength of 800 nm. The laser adheres to typical parameters resembling a 200 TW tabletop laser system with fixed energy ( $E_L = 5 \text{ J}$ ) and duration (FWHM of the intensity)  $\tau_i = 25 \text{ fs}$ , which is also observed in the CLAPA laser when operating at full power. The laser is vertically incident from the left boundary ( $x = 0$ ) of the  $60 \mu\text{m} \times 30 \mu\text{m} \times 30 \mu\text{m}$  simulation box. This box employs a grid of  $3000 \times 60 \times 60$  cells. The plasma target, comprising electrons and carbon, exists at  $x \geq 10 \mu\text{m}$ . Along the propagation direction, the electron density increases linearly from 0 at  $x = 10 \mu\text{m}$  to  $n_e = n_0$  at  $x = 20 \mu\text{m}$ , varying  $n_0$  from  $0.005n_c$  to  $0.5n_c$  in different simulations, where  $n_c$  is the critical density. For each species, eight macroparticles per cell are loaded in the areas where the plasma density is above zero. The simulation box, acting as a moving window,

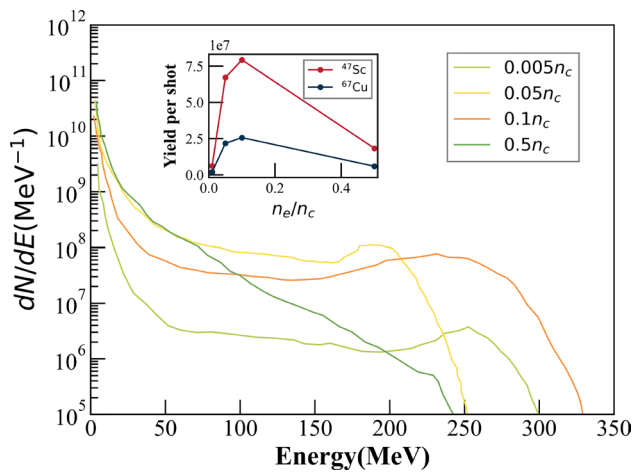


**Fig. 5** (Color online) Electron spectra of different plasma densities when a 200 TW laser focuses on the matching spot size. The sub-figure illustrates the enhanced isotope yield under various electron acceleration schemes

begins moving at a constant velocity  $v_\omega = 0.996c$  when the simulation time  $t_\omega$  surpassed 200 fs. The spot size is calculated by substituting  $E_L$  and  $\tau_i$  into Eq. 5.

The simulation results are shown in Fig. 5. We observed that at a plasma density of  $0.5n_c$ , the dominant electron acceleration mechanism is the direct laser acceleration mechanism, characterized by a large charge but relatively low energy, whereas at  $0.005n_c$ , the dominant mechanism is the LWFA, which achieves a peak at higher energy levels but with a lower charge. As discussed in the previous section, the isotope yield increased linearly with charge and logarithmically with energy. If these two factors cannot simultaneously achieve their maximum values, we aim to make the right trade-off to maximize the yield. At  $0.1n_c$ , a hybrid acceleration mechanism combining LWFA and DLA enables a significant charge and relatively high energy in the electrons. When these electron energy spectra were inputted into Geant4 for the simulation, the  $0.1n_c$  condition resulted in the maximum yield. Setting the converter thickness to 12 mm according to Fig. 2 generated  $7.9 \times 10^7$   $^{47}\text{Sc}$  and  $2.6 \times 10^7$   $^{67}\text{Cu}$  per laser shot. Compared with the results in the previous section, the yield increased by more than tenfold.

Figure 6 depicts the cumulative activity obtained as a function of irradiation time with the laser frequency set at 10 Hz. After irradiation for three half-lives, the activities of both isotopes surpassed 95% of their maximum values, indicating that, under optimal conditions of electron acceleration and target material parameters, both isotopes can achieve the dosage required for PET diagnostics using this regime. In particular,  $^{47}\text{Sc}$  required a shorter duration of approximately 50 h, whereas  $^{67}\text{Cu}$  required a longer duration of approximately 180 h. Moreover, the maximum

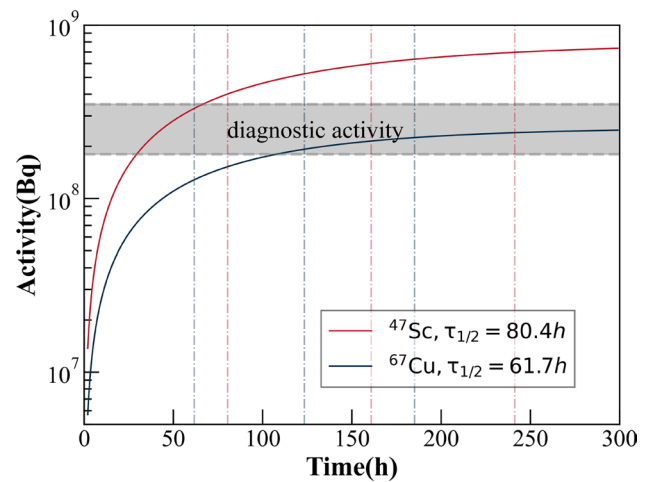


**Fig. 6** (Color online) Accumulated activity varied with radiation time when a repetition rate of 10 Hz is employed. The gray area represents the typical dose required for PET diagnosis. The vertical dashed lines indicate the half-life of the corresponding color-coded isotope

activity of  $^{47}\text{Sc}$  reached 0.8 GBq. By employing multiple lasers simultaneously or utilizing lasers with higher repetition rates, this laser-induced generation approach could potentially satisfy the activity levels required for therapeutic purposes, whose activity requirements generally range from several GBq to tens of GBq.

## 5 Conclusion

Our research confirms the viability of using laser-induced  $(\gamma, p)$  reactions for the production of  $^{47}\text{Sc}$  and  $^{67}\text{Cu}$  isotopes, representing a significant step toward environmentally friendly and cost-effective medical isotope generation. The compactness of high-intensity laser systems enables decentralized production, addressing the logistical challenges of isotope transportation, and minimizing radioactive waste. The precise control over the reaction zone ensures the high specific activity of the produced isotopes, which is crucial for medical applications.

Given that stable long-term kHz operations of LWFAs have already been reported [29] and an increasing number of high-charge laser electron acceleration experiments have been conducted [30], laser-induced  $(\gamma, p)$   $^{47}\text{Sc}$  and  $^{67}\text{Cu}$  generation holds significant potential. If, in the future, electron acceleration in NCD plasma can be combined with kHz lasers, the diagnostic activity can be reached within a few hours and therapeutic doses of medical isotopes can be generated. The methodology employed in this study can be readily extended to other photonuclear reactions.

**Author Contributions** All authors contributed to the study conception and design. Material preparation, data collection and analysis were performed by Jian-Yao Zhang, Di Wu and Hao-Yang Lan. The first draft of the manuscript was written by Jian-Yao Zhang and all authors commented on previous versions of the manuscript. All authors read and approved the final manuscript.

**Data availability** The data that support the findings of this study are openly available in Science Data Bank at <https://cstr.cn/31253.11.sciencedb.j00186.00257> and <https://www.doi.org/10.57760/sciencedb.j00186.00257>.

## Declarations

**Conflict of interest** The authors declare that they have no conflict of interest.

## References

- H.W. Wang, G.T. Fan, L.X. Liu et al., Commissioning of laser electron gamma beamline SLEGS at SSRF. *Nucl. Sci. Tech.* **33**, 87 (2022). <https://doi.org/10.1007/s41365-022-01076-0>
- Z. Ma, H. Lan, W. Liu et al., Photonuclear production of medical isotopes  $^{62,64}\text{Cu}$  using intense laser-plasma electron source. *Matter Radiat. Extremes* **4**, 064401 (2019). <https://doi.org/10.1063/1.5100925>
- W.T. Pan, T. Song, H.Y. Lan et al., Photo-excitation production of medically interesting isomers using intense-ray source. *Appl. Radiat. Isotopes* **168**, 109534 (2021). <https://doi.org/10.1016/j.apradiso.2020.109534>
- Z. Cao, W. Qi, H. Lan et al., Experimental study of medical isotopes  $^{62,64}\text{Cu}$  and  $^{68}\text{Ga}$  production using intense picosecond laser pulse. *Plasma Phys. Control. Fusion* **65**, 055007 (2023). <https://doi.org/10.1088/1361-6587/ac9090>
- X.L. Wang, Z.Y. Xu, W. Luo et al., Transmutation prospect of long-lived nuclear waste induced by high-charge electron beam from laser plasma accelerator. *Phys. Plasmas* **24**, 093105 (2017). <https://doi.org/10.1063/1.4998470>
- M.G. Lobok, A.V. Brantov, V.Y. Bychenkov, Laser-based photonuclear production of medical isotopes and nuclear waste transmutation. *Plasma Phys. Control. Fusion* **64**, 054002 (2022). <https://doi.org/10.1088/1361-6587/ac53f0>
- X.L. Wang, Z.Y. Tan, W. Luo et al., Photo-transmutation of long-lived radionuclide  $^{135}\text{Cs}$  by laser-plasma driven electron source. *Laser Part. Beams* **34**, 433–439 (2016). <https://doi.org/10.1017/S0263034616000318>
- H.Y. Lan, D. Wu, J.X. Liu et al., Photonuclear production of nuclear isomers using bremsstrahlung induced by laser-wakefield electrons. *Nucl. Sci. Tech.* **34**, 74 (2023). <https://doi.org/10.1007/s41365-023-01219-x>
- F. Kitatani, H. Harada, S. Goko et al., Measurement of  $^{76}\text{Se}$  and  $^{78}\text{Se}$  ( $\gamma$ , n) cross sections. *J. Nucl. Sci. Technol.* **48**, 1017–1024 (2011). <https://doi.org/10.1080/18811248.2011.9711787>
- K.Y. Hara, H. Harada, F. Kitatani et al., Measurements of the  $^{152}\text{Sm}(\gamma, n)$  cross section with laser-compton scattering  $\gamma$  rays and the photon difference method. *J. Nucl. Sci. Technol.* **44**, 938–945 (2007). <https://doi.org/10.1080/18811248.2007.9711333>
- D. Wu, H.Y. Lan, J.Y. Zhang et al., New measurements of  $^{92}\text{Mo}(\gamma, n)$  and  $(\gamma, 3n)$  reactions using laser-driven bremsstrahlung  $\gamma$ -ray. *Front. Phys.* **11**, 1178257 (2023). <https://doi.org/10.3389/fphy.2023.1178257>
- M.Z. Wang, D. Wu, H.Y. Lan et al., Cross section measurements of  $^{27}\text{Al}(\gamma, x)^{24}\text{Na}$  reactions as monitors for laser-driven bremsstrahlung  $\gamma$ -ray. *Nucl. Phys. A* **1043**, 122834 (2024). <https://doi.org/10.1016/j.nuclphysa.2024.122834>
- B.S. Nunes, E.R.F. Rodrigues, J.A.P. Fruscalzo et al., Highly enriched uranium-free medical radioisotope production methods: an integrative review. *Appl. Sci.* **12**, 12569 (2022). <https://doi.org/10.3390/app122412569>
- A.G. Kazakov, T.Y. Ekatoeva, J.S. Babenya, Photonuclear production of medical radiometals: a review of experimental studies. *J. Radioanal. Nucl. Ch.* **328**, 493–505 (2021). <https://doi.org/10.1007/s10967-021-07683-2>
- S. Howard, V.N. Starovoitova, Target optimization for the photonuclear production of radioisotopes. *Appl. Radiat. Isotopes* **96**, 162–167 (2015). <https://doi.org/10.1016/j.apradiso.2014.12.003>
- Z. Sun, Review: production of nuclear medicine radioisotopes with ultra-intense lasers. *AIP Adv.* **11**, 040701 (2021). <https://doi.org/10.1063/5.0042796>
- C. Müller, M. Bunka, S. Haller et al., Promising prospects for  $^{44}\text{Sc}$ -/ $^{47}\text{Sc}$ -based theragnostics: application of  $^{47}\text{Sc}$  for radionuclide tumor therapy in mice. *J. Nucl. Med.* **55**, 1658–1664 (2014). <https://doi.org/10.2967/jnumed.114.141614>
- L. Mou, P. Martini, G. Pupillo et al.,  $^{67}\text{Cu}$  production capabilities: a mini review. *Molecules* **27**, 1501 (2022). <https://doi.org/10.3390/molecules27051501>
- A.C. Reyes, The implementation of indigenous peoples education (IPED) program: towards a proposed plan of action. Proceedings of the Asia Pacific of the Asia Pacific Conference on Multidisciplinary Research (APCMR), 30–31 July 2022. pp. 13–24 <https://doi.org/10.54476/apjaet/69215>
- G. Hovhannisyanyan, T. Bakhshiyanyan, R. Dallakyan, Photonuclear production of the medical isotope  $^{67}\text{Cu}$ . *Nucl. Instrum. Methods Phys. Res. Sect. B* **498**, 48–51 (2021). <https://doi.org/10.1016/j.nimb.2021.04.016>
- I. Novak-Hofer, A.P. Schubiger, Copper-67 as a therapeutic nuclide for radioimmunotherapy. *Eur. J. Nucl. Med. Mol. Imag.* **29**, 821–830 (2002). <https://doi.org/10.1007/s00259-001-0724-y>
- J.M. Walshe, G. Potter, The pattern of the whole body distribution of radioactive copper ( $^{67}\text{Cu}$ ,  $^{64}\text{Cu}$ ) in Wilson's disease and various control groups. *QJM Int. J. Med.* **46**, 445–462 (1977). <https://doi.org/10.1093/oxfordjournals.qjmed.a067518>
- A.J. Koning, D. Rochman, Modern nuclear data evaluation with the TALYS code system. *Nucl. Data Sheets* **113**, 2841–2934 (2012). <https://doi.org/10.1016/j.nds.2012.11.002>
- S. Agostinelli, J. Allison, K. Amako et al., Geant4—a simulation toolkit. *Nucl. Instrum. Methods Phys. Res. Sect. A* **506**, 250–303 (2003). [https://doi.org/10.1016/S0168-9002\(03\)01368-8](https://doi.org/10.1016/S0168-9002(03)01368-8)
- T. Tajima, X.Q. Yan, T. Ebisuzaki, Wakefield acceleration. *Rev. Mod. Plasma Phys.* **4**, 7 (2020). <https://doi.org/10.1007/s41614-020-0043-z>
- W. Song, R.H. Hu, Y.R. Shou et al., High-yield high-efficiency positron generation in high-z metal targets irradiated by laser produced electrons from near-critical density plasmas. *Chin. Phys. Lett.* **34**, 085201 (2017). <https://doi.org/10.1088/0256-307X/34/8/085201>
- W. Lu, M. Tzoufras, C. Joshi et al., Generating multi-gev electron bunches using single stage laser wakefield acceleration in a 3D nonlinear regime. *Phys. Rev. ST Accel. Beams* **10**, 061301 (2007). <https://doi.org/10.1103/PhysRevSTAB.10.061301>
- J. Derouillat, A. Beck, F. Pérez et al., Smilei: a collaborative, open-source, multi-purpose particle-in-cell code for plasma simulation. *Comput. Phys. Commun.* **222**, 351–373 (2018). <https://doi.org/10.1016/j.cpc.2017.09.024>
- L. Rovige, J. Huijts, I. Andriyash et al., Demonstration of stable long-term operation of a kilohertz laser-plasma accelerator. *Phys. Rev. Accel. Beams* **23**, 093401 (2020). <https://doi.org/10.1103/PhysRevAccelBeams.23.093401>

30. J. Liu, H. Lu, H. Lu et al., Generation of 400 pC electron bunches in laser wakefield acceleration utilizing a structured plasma density profile. *Phys. Plasmas* **30**, 113103 (2023). <https://doi.org/10.1063/5.0161811>

author(s) or other rightsholder(s); author self-archiving of the accepted manuscript version of this article is solely governed by the terms of such publishing agreement and applicable law.

Springer Nature or its licensor (e.g. a society or other partner) holds exclusive rights to this article under a publishing agreement with the